POSS Enhanced 3D Graphene - Polyimide Film for Atomic Oxygen Endurance in Low Earth Orbit Space Environment.

Ranjana Shivakumar [a], Asaf Bolker [b], Siu Hon Tsang [c,], Nurit Atar [b], Ronen Verker [b], Irina Gouzman [b], Mor Hala [b], Nehora Moshe [b], Alexandra Jones [d], Eitan Grossman [b], Timothy K. Minton [d], and Edwin Hang Tong Teo [a]*

[a] School of Electrical and Electronic Engineering, Nanyang Technological University, 50 Nanyang Avenue, 639798, Singapore.

[b] Space Environment Department, Soreq NRC, Yavne 81800, Israel.

[c] Temasek Laboratories@NTU, 50 Nanyang Avenue, 639798, Singapore.
E-mail: SHTSANG@ntu.edu.sg

[d] Department of chemistry and biochemistry, 103 chemistry biochemistry building, Montana state university, Bozeman, MT 59715, United States.

Abstract

Recently, 3D-graphene infused polyimide (3DC/PI) films have shown to be an effective protection coating for electrostatic discharge in spacecraft. However, these films are not suitable for Low Earth Orbit (LEO) due to atomic oxygen (AO) erosion. Here, we used Polyhedral Oligomeric Silsesquioxane (POSS) to enhance the AO durability of 3D-C/PI films. Three different ways of adding POSS to the composite films were studied with ground-based AO exposure. For all infusion approaches, their electrical conductivity behaviour is well preserved and the presence of POSS results in reduced AO erosion yield. Of all the methods studied here, incorporating POSS directly into PI results in the lowest erosion yield of 4.67×10^{-25} cm^3/O-atom (one order of magnitude lower than that of Kapton). Adding POSS to PI, extends the durability of the composite film beyond 10 years, making it an ideal protective material for long term mission in LEO.

Keywords: 3D-C foams, POSS, Polyimide, nanocomposites, atomic oxygen, Low Earth Orbit.

1. Introduction:

Satellites for long term space missions are typically launched to low Earth orbit (LEO, at 200 - 800 km altitude) and geosynchronous equatorial orbit (GEO, at 35,786 km altitude) which are characterized by harsh environmental conditions such as atomic oxygen (AO) (at LEO only), ultraviolet (UV) and ionizing radiation, plasma, extreme thermal cycles (-120 °C to 120 °C every orbital cycle), vacuum, impact by micrometeoroids, and space debris [1-4]. Almost 25% of spacecraft failure modes, are linked to interactions with outer space environment [5]. Space qualified polyimides (PIs), such as Kapton, are generally used in thermal blanket for satellites (external layers in multilayer insulation, MLI)[6] to protect them from outer space environment. Despite having high thermal stability, elastic modulus and tensile strength [7], PIs are vulnerable to AO erosion at LEO and electrostatic discharge (ESD) in LEO and mostly in GEO.

The ESD and AO erosion of the PIs, are usually mitigated by applying protective coatings on the outer layer. Conductive coating made of indium tin oxide (ITO) is used for ESD protection. Protective coatings such as Al_2O_3, SiO_2, S_nO_2, or ITO [8-11], are used to reduce AO erosion. However, these coatings are very brittle and are prone to crack upon folding or bending, even to a small extent, resulting in increased sheet electrical resistance [12]. In addition, they are also vulnerable to damage by micrometeoroids and space debris. Once the crack is formed, the underlying substrate is subjected to AO attack, leading to erosion [8, 12]. Another method for AO protection, is by adding fillers (nanomaterials) as additives [13-16] or by tweaking polymer backbone [17-19]. These nanofillers, tend to cause inhomogeneous distribution, affecting the structural integrity of the polymer matrix [20, 21].

In a previous work, three-dimensional (3D) Graphene foam (3D-C) [22-24] was infused as filler in the PI to mitigate electrostatic discharge. A new method was developed, to obtain 3D-C infused PI for space applications to prevent ESD build-up [25-27]. Adding 3D-C as filler material helped to overcome the disadvantage associated with other fillers such as inhomogeneous distribution. In addition, due to its interconnected structure, a very low filling fraction is required to enhance the thermal and electrical conductivity of the PI. 3D-C/PI demonstrated good compatibility with GEO environment. However, 3D-C/PI film cannot be used in LEO, where AO exposure is known to have a dominating effect on the space materials leading to oxidation, surface erosion and mass loss and is of greater concern for long-term missions [28]. The composite is expected to erode under long term AO exposure at LEO altitudes. Carbon-based materials, e.g. 3D-C and PI are susceptible to erosion due to collision with AO at a high relative velocity (5 eV), both in LEO and in laboratory testing [29]. For example, PIs such as Kapton® have a high erosion yield of 3×10^{-24} cm^3/O-atom when exposed to AO and are commonly used for assessing the AO flux in LEO ground simulation facilities [30]. Thus, 3D-C/PI film cannot be used in LEO environment, without any protection against AO attack.

The objective of this work is to improve the AO durability of 3D-C/PI films and for this Polyhedral oligomeric silsesquioxane (POSS), an organic-inorganic hybrid, has been used. POSS has a cubic cage-like molecular structure, made of inorganic Si-O-Si framework (0.53 nm side length), surrounded by up to eight organic groups with the empirical formula $(RSiO_{1.5})_n$. POSS, which has already been used in a wide range of applications such as electronics, biological

systems and aerospace [31-35] is being incorporated both in polymers and carbon nanostructures to improve their properties. Copolymerization, or incorporating POSS in polymer functional groups helps to resist AO induced degradation [36-40]. It was found that when exposed to AO the POSS organic groups are etched away and a surface SiO_2 passivation layer is formed to protect the polymer from further O-atom attack [41]. In addition, studies show that, adding POSS into polymer matrices helps to improve their thermal stability, mechanical strength, viscosity, impact and chemical resistance [42, 43]. In a recent work, Trisilanolphenyl (TSP)-POSS was added to intrinsically AO-resistive phosphorous-containing PI film (FPI) to further enhance the AO durability for long term applications. It was shown that 25 wt% of TSP-POSS could significantly reduce the AO erosion yield to about 5.8% of that of FPI film.[44] POSS nanoparticles were also chemically grafted (functionalization) on to different carbon surfaces such as graphene, carbon nanotube [45], carbon dots [46], graphene oxide film [47], carbon fibre [48], and fullerenes, to improve the properties of the composite structures, and for various other applications [49-53]. Hence, in this work, both ways of adding POSS to the composite film have been explored, to find the optimized method of AO protection using POSS. In any composite structure, the mechanical behaviour and environmental stability depends greatly on the matrix itself and the interface between the matrix and reinforcement [54-56]. These properties can be enhanced by appropriately engineering the interface [57-59], to relieve internal stress concentrations, or by tweaking polymer backbone. Moreover, it is essential to observe the effect that the addition of POSS in various ways has on the composite mechanical properties.

In the present work, three different methods were utilized for adding POSS to 3D-C/PI and the resulting hybrid films: 3D-C-POSS/PI (POSS in 3D-C alone), 3D-C/PI-POSS (POSS incorporated in PI alone) and 3D-C-POSS/PI-POSS (POSS incorporated in both 3D-C and PI) were studied and compared. An optimised process, to improve the AO durability of 3D-C/PI has been identified by comparing the sample properties. These POSS containing composite films, along with 3D-C/PI films were subjected to ground-based AO exposure, to access their durability in LEO. In addition, the effect of POSS on the electrical and mechanical properties of the samples were studied and compared. Pyromellitic dianhydryde-oxydianiline (PMDA-ODA) polyamic acid blends with different concentration of TSP-POSS were infused into the 3D-C based foams [60]. Additionally, we have incorporated 3D-C with aminopropyl isobutyl POSS (NH_2-POSS) for the first time resulting in the entire surface of all the branches of 3D-C to be uniformly covered with NH_2-POSS nanoparticles. The POSS nanoparticles are physically absorbed on the 3D-C surface forming a 3D-C-POSS composite foam structure. It was demonstrated in the earlier work, that infusing PI with 3D-C helps to avoid the ESD build up [27], and in this work AO durability of 3D-C/PI is improved by adding POSS with no detrimental effect on the electrical properties. We have demonstrated that, adding TSP-POSS to the PI results in a composite film with good AO resistance along with higher mechanical properties proving to be suitable for long term space applications. A slight reduction in the stiffness of the films compared to that of pure PI is observed. Weak physical bond between 3D-C and POSS in addition to poor PI infiltration inside the 3D-C branches are suspected to reduce the stiffness of the films lower than that of pure PI. However, the composite samples are potentially suited for use as the outer layer of thermal blankets in satellites as they undergo mostly bending and only a minor tensile stress. For other applications, optimization of PI matrix and the bonding between 3D-C and POSS should be explored.

2. Experimental Section:

2.1. Materials

The materials studied in this work are 3D-C foam, TSP-POSS-PI matrix blend and AminoproylIsobutyl POSS (POSS-NH_2). POSS-NH_2 was purchased from Alfa Chemistry (USA) as crystalline powder and used as received. Tetrahydrofuran, anhydrous (THF) was purchased from Sigma Aldrich (401757). Polyamic acid (PAA) solution of 15 wt% PMDA-ODA in N-methyl-2-pyrrolidone (NMP) was purchased from Sigma-Aldrich (575801) to form the pristine PI matrix. Blends containing 5 and 15 wt% TSP-POSS in PAA were purchased from Hybrid Plastics (PM1215.5 and PM1215.15, respectively) to form the TSP-POSS-PI matrices.

2.2. Preparation of 3D-C

The three-dimensional interconnected graphene foam-like structure (3D-C) was obtained by template assisted direct thermal chemical vapour deposition (TCVD). Nickel (Ni) foam was used as a template and catalytic substrate. The Ni foam was annealed at 1000 °C in a quartz tube placed inside TCVD furnace under constant Ar and H_2 flow. Annealing is done to clean the Ni surface and to remove the oxide layer from the Ni surface. After annealing for about 5 minutes a small amount of methane (CH_4) was introduced into the tube following decomposition of methane and deposition of graphene film on the surface of Ni foam. The whole synthesis process was carried out under ambient pressure and after the growth period the samples were subjected to rapid cool down to room temperature under constant Ar and H_2 flow. The flow rate of CH_4 and the growth time depends on the concentration of total gas flow and the Ni foam dimensions. 3D-C/Ni sample was then dip-coated with poly (methyl methacrylate) (PMMA) and heated to protect the 3D-C structure while etching the Ni substrate. Once the PMMA has hardened forming a protective film on the graphene surface, the samples were treated with hot dilute hydrochloric acid (HCl) for about 3 to 5 hours or until the Ni substrate has been completely etched off. Freestanding, ultralight and flexible graphene foam was then obtained by annealing the samples for 1 h at 700 °C in Ar and H_2 atmosphere in order to remove the PMMA [22, 23, 27].

2.3. Preparation of 3D-C-POSS

POSS-NH_2 was incorporated into the as grown freestanding 3D-C foams as shown schematically in **Figure 1**. THF was used as a solvent in order to disperse POSS-NH_2 agglomerates and to provide a medium for attaching the POSS-NH_2 to the 3D-C foam surface. A small quantity of POSS-NH_2 powder was added to THF and mixed by ultra-sonication in an ultrasonic bath for about 15 minutes. This helps to disperse or de-agglomerate the POSS particles in the solvent. The fabricated 3D-C foams were then immersed in the solution and heated at 50 °C for about 4 hours. The foams were then removed, washed with DI water and dried by heating at 110 °C for 30 minutes. The result is a POSS coated 3D-C foam structure.

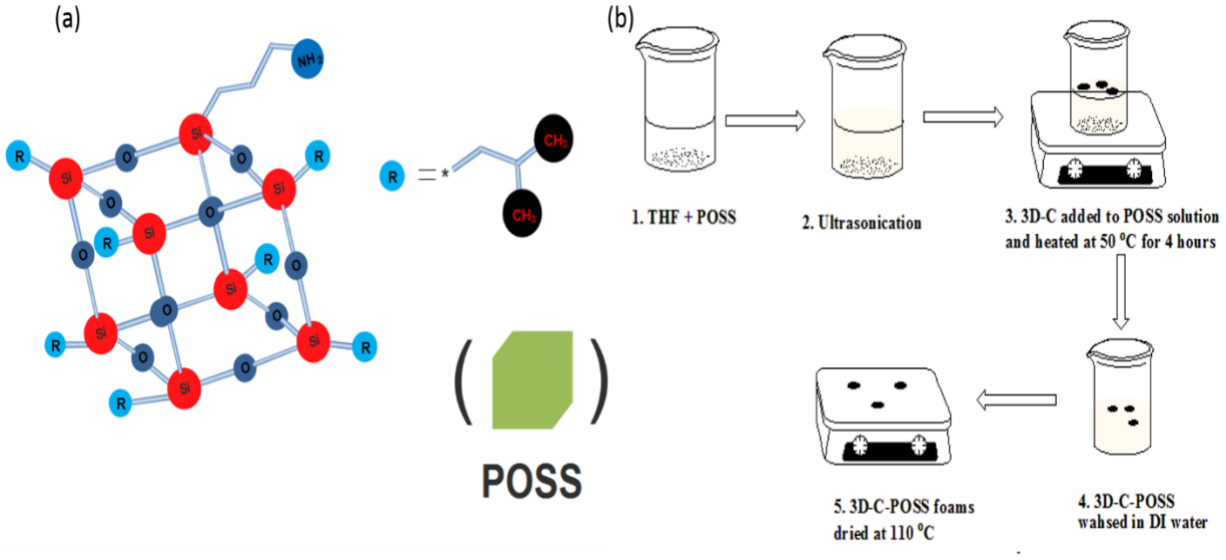

Figure 1. Schematic of the POSS-NH_2 used and its incorporation into 3D-C. a) POSS-NH_2 molecular structure showing eight organic groups attached to the cubic Si-O-Si (inorganic) framework (Si atom - red, O atom - dark blue and organic group - light blue); b) Schematic illustration of POSS-NH_2 incorporation onto 3D-C. 3D-C foams are first grown by template assisted Chemical Vapour Deposition on a Ni substrate and then POSS-NH_2 is incorporated using THF as a solvent. The samples are then washed in DI water to remove excess POSS and dried to obtain 3D-C-POSS foams.

2.4. Preparation of 3D-C-POSS/PI Nanocomposite

Neat PAA solution and PAA blends with 5, and 15 wt % TSP-POSS content were infiltrated into the 3D-C foams. The composite materials were formed by PAA solution curing into PI under gradual heating to 350 °C in nitrogen atmosphere, based on previously published procedure [27]. For this study, four types of composite samples were prepared by adding POSS to 3D-C and/or PI as follows: 3D-C-POSS/PI, 3D-C-POSS/PI-POSS, 3D-C/PI-POSS and 3D-C/PI (no POSS). POSS-NH_2 is added to 3D-C and TSPPOSS is added to the PI.

2.5. Morphological and Chemical Characterization

Scanning electron microscopy (SEM) was used to take images of 3D-C before and after adding POSS using, JEOL JSM-IT100. Additional SEM images were taken before and after the exposure of the various composites to AO using, Zeiss Sigma 300 VP. Fourier transform infrared (FTIR) spectroscopy measurements were performed in the range of 400 – 4000 cm^{-1} in absorbance mode using Shimadzu IRPrestige-21 to investigate the chemical composition. Raman spectroscopy (UHT S300 & WITEC CRM200 Raman with an Nd:YAG 532 nm laser as excitation source) was performed at room temperature. X-ray photo electron spectroscopy (XPS) measurements were used to assess the surface chemical composition. Survey scan was made to determine the detectable elements and high-resolution spectra were obtained for C 1s for both 3D-C and 3D-C-POSS. Thermogravimetric analysis was done using Shimazdu Scientific Instruments DTG-60H with a heating rate of 10 °C /minute under dry air atmospheric condition.

2.6. Atomic-Oxygen Exposure

Ground based AO exposure of the composite films were carried out using a laser detonation hyperthermal AO pulsed beam [61]. The oxygen atoms in the AO beam were generated by breaking down O_2 gas in a conical nozzle using a CO_2 laser with 7 J/pulse. The composite films were cut into required dimensions and attached to Si substrate with an aluminum foil. They were exposed to AO fluences of 7.18×10^{19} O-atom/cm^2 and 2.72×10^{20} O-atom/cm^2 and their mass loss was plotted against AO fluence. The erosion yield E (cm^3 / O-atom), of the composite was calculated as per ASTM E2089, standard testing method [62].

(1)
$$E = \frac{\Delta m}{A\rho F}$$

Where,
Δm = Mass loss (g)
A = Exposed area (cm^2)
ρ = Density of the sample (g cm^{-3})
F = Atomic oxygen fluence (O-atoms/cm^2), determined from the erosion of Kapton-H reference sample [61].

Δm of the exposed composites was measured using a microbalance (Sartoruis SE2 – readability of 0.1 μg). The AO fluence was determined from etch depth measurement of a Kapton-H reference sample using a profilometer. The LEO equivalent AO fluence was then calculated using equations (1) and (2), the measured Kapton-H etch depth and its known erosion yield, 3×10^{-24} cm^3/O-atom.

(2)
$$\Delta d = \frac{\Delta V}{A} = \frac{\Delta m/\rho}{A}$$

Where, Δd is the etch depth (cm) and ΔV is the etched volume (cm^3).

2.7. Electrical Characterization

Electrical resistivity of the composite samples was measured using the same method as described in the literature [27, 35]. Van der Pauw four-point probe method was used to measure the temperature dependent electrical conductivity [63]. This method eliminates the effect of contact resistance and sample geometry. A THMS600 Linkam stage was used to control the sample temperature in N_2 atmosphere. Current was applied and measured using a Keithley 220 programmable current source and Keithley 485 picoammeter respectively. Silver paint dots were spread on the four corners of the sample surface to apply electrical contacts on the four points. This non-destructive method prevented any substantial damage to the sample surface. A very high input impedance (>200TΩ) Keithley 6514 electrometer was connected to each of the four contact points. A Keithley 2000 multimeter was used to measure the voltage difference between each of the two electrometers. The current source, electrometers, multimeter, and sample

contacts were connected to a Keithley 7001 switch. Samples were tested before and after AO exposure.

2.8. Mechanical Characterization

The mechanical properties of the films where measured using dynamic mechanical analysis (DMA, TA Instruments Q800), at a temperature of 30 ^{o}C and a force ramp rate of 0.1 N/min. The samples were cut into 20 mm × 4 mm rectangular shapes and five samples of each type were measured. Stress strain curves were obtained during a tension test.

3. Results and Discussion

3.1. Morphological and Chemical Characterization

The surface morphology of 3D-C-POSS structure was observed by SEM. The top view SEM images presented in **Figure 2**, shows the free-standing graphene foams and it can be seen in the low magnification view images that the POSS-NH_2 is incorporated on the surface of the 3D-C foams. POSS agglomerates of various sizes are clearly visible, coating almost the entire surface of the 3D-C. The structure of the foam is preserved even after adding POSS.

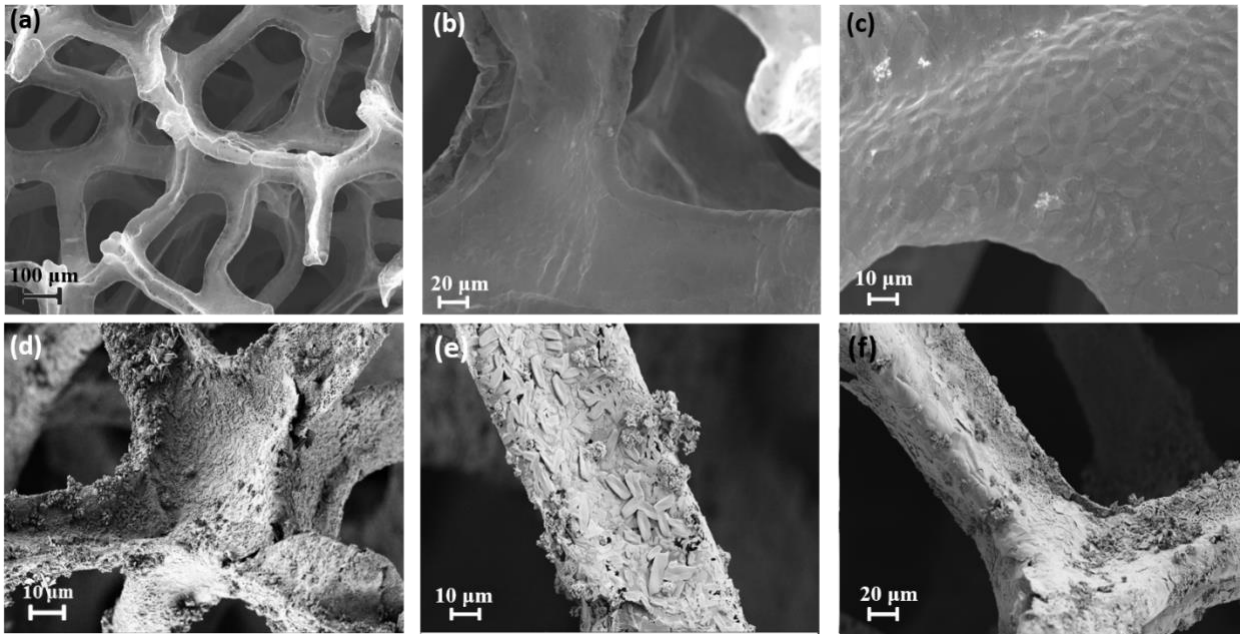

Figure 2. Scanning electron microscopy. a-c) SEM images of 3D-C showing 3D interconnected foam like structure and a smooth surface; **d-e)** SEM images of 3D-C after treating with POSS-NH_2 in THF solution showing the coating of POSS-NH_2 on the foam surface. It can be seen that the POSS-NH_2 agglomerates cover almost the entire surface of the foam branches.

Surface functional group analysis was performed by FTIR spectroscopy. **Figure 3a** shows the FTIR spectra for 3D-C, POSS-NH_2 and 3D-C-POSS hybrid structure. Bonds of absorbed carbon dioxide from air can be seen in all the samples. The small peak at 2800 cm^{-1} in 3D-C foam can

be attributed to C-H, indicating that the graphene foam is H- terminated as Ar and H_2 were used as carrier gas for synthesis in the TCVD system. The FTIR spectra of POSS-NH_2 shows a strong peak at 1110 cm^{-1}, corresponding to Si-O-Si bond in POSS cage structure. Strong double peaks due to C-H stretching of the CH_2 groups in the organic groups (R) were also observed in the range of 2873-2960 cm^{-1}. The C-N bond stretching causes the band at 1223 cm^{-1} conforming the amine group in POSS. The peak for Si-C bond at 1230 cm^{-1} can also be seen. Similarly, the FTIR spectra for 3D-C-POSS shows the strong peak at 1110 cm^{-1} and correspondingly weak bands over 2750-3000 cm^{-1} (due to the isobutyl groups in POSS), signifying the absorption of POSS onto graphene foam. There is also a broad band in the range of 3200 to 3600 cm^{-1} corresponding to O-H and N-H stretching vibrations [64]. The FTIR results prove that POSS-NH_2 is embedded on the 3D-C surface through van der waals bonding. Raman spectra of 3D-C, POSS-NH_2 and 3D-C-POSS is presented in **Figure 3b**. G-peak and 2D peak can be seen for pure 3D-C sample. The intensity of the G-peak is about two times the intensity of the 2D peak indicating multi-layer graphene [65, 66]. It can be seen from the Raman spectra of 3D-C-POSS that the characteristic band of C-H functional group belonging to POSS spectra is also present in 3D-C-POSS spectrum conforming that the POSS has been physically absorbed on the 3D-C surface.

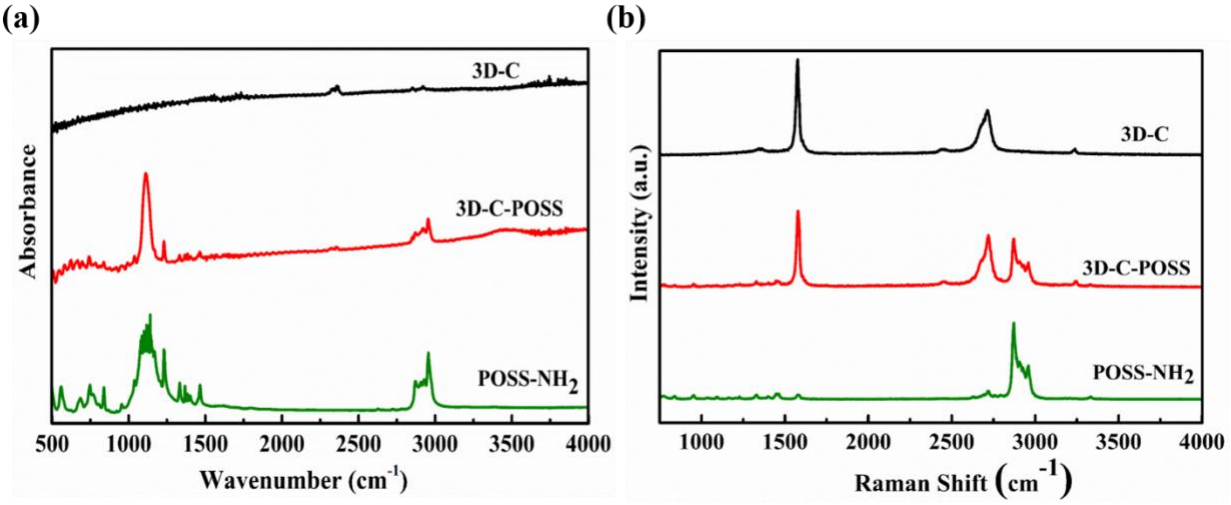

Figure 3. a) FTIR spectra of 3D-C (black, top) before the incorporation of POSS nanoparticles, 3D-C-POSS (red, middle) and POSS-NH_2 powder (green, bottom). FTIR spectra for 3D-C-POSS displays a strong peak at 1110 cm^{-1} (Characteristic of Si-O-Si stretching band) and comparatively week bands over 2750-3000 cm^{-1} (characteristic of isobutyl groups in POSS-NH_2) due to POSS nanoparticles [64]; b) Raman spectroscopy of 3D-C, POSS-NH_2, and 3D-C-POSS. The Raman band in the range of 2800 to 3000 cm^{-1} indicates the presence of C-H functional group in 3D-C-POSS.

Thermogravimetric analysis (TGA) was used to measure the thermal stability of 3D-C, POSS-NH_2 and 3D-C-POSS. **Figure 4a** shows the sample weight as a function temperature for the three samples from room temperature to about 1100 °C under dry air atmosphere. POSS follows two step thermal degradation in air, in which evaporation and oxidation competes with each other. This complex phenomenon results in a residue that is thermally stable. In other words, oxidation take place in the organic chains and produces ceramic, silica-like phase as a result of

cage crosslinking [67]. The initial weight loss for POSS-NH_2 occurs at 250 °C and fully subsides by 375 °C. This is due to the incomplete decomposition (evaporation) of organic segments in the POSS molecule. This is followed by oxidation in the organic chains leaving a residue of ~ 38% at 1000 °C. From the TGA curve of 3D-C, it can be seen that there is a minor weight loss region (3 to 4% below 300 °C) followed by major weight loss. This is due to the evaporation of absorbed water and oxygen decomposition of surfactant residue. The primary decomposition (complete oxidation of carbon) of 3D-C takes place at 803 °C. Complete weight loss for 3D-C is attributed to its purity [68]. The thermogravimetric profile of 3D-C-POSS is characterized by an initial 3% weight loss up to 200 °C due to thermal desorption of absorbed water molecules on the foam surface followed by ~20% weight loss at ~ 300 °C due to POSS cage oxygen decomposition. The higher weight loss associated with oxygen decomposition in 3D-C-POSS compared to 3D-C can be attributed to the oxygen group in POSS molecules. 3D-C-POSS shows a residual weight of around 25% at 1000 °C, which can be recognized to be due to the formation of dense Si-O structure resulting from partial crosslinking of the POSS cages. This residue after TGA was subjected to FTIR analysis and the absorbance spectra is shown in **Figure 4b** in comparison to the spectra of 3D-C-POSS before TGA. It can be seen that Si-O-Si peak at 1110 cm^{-1} has shifted to 1090 cm^{-1} indicating the formation of Si-O structure as a result of partial cross linking of POSS cages [67, 69]. From the TGA analysis it is clear that the thermal stability of 3D-C has not been altered by the addition of POSS particles.

Similar TGA curves (**Figure S1**) and FTIR spectra (**Figure S2**) were obtained for the composite samples (3D-C/PI, 3D-C-POSS/PI, 3D-C/PI-POSS and 3D-C-POSS/PI-POSS). Si-O residue is seen for the composite films that contained POSS. This was confirmed by the Si-O stretching band at 1090 cm^{-1} in the FTIR absorbance spectra. In addition, the TGA measurements show that the composite samples with POSS content in the PI (3D-C/PI-POSS and 3D-C-POSS/PI-POSS) have more Si-O residue indicating the higher amount of POSS in these films compared to 3D-C-POSS/PI.

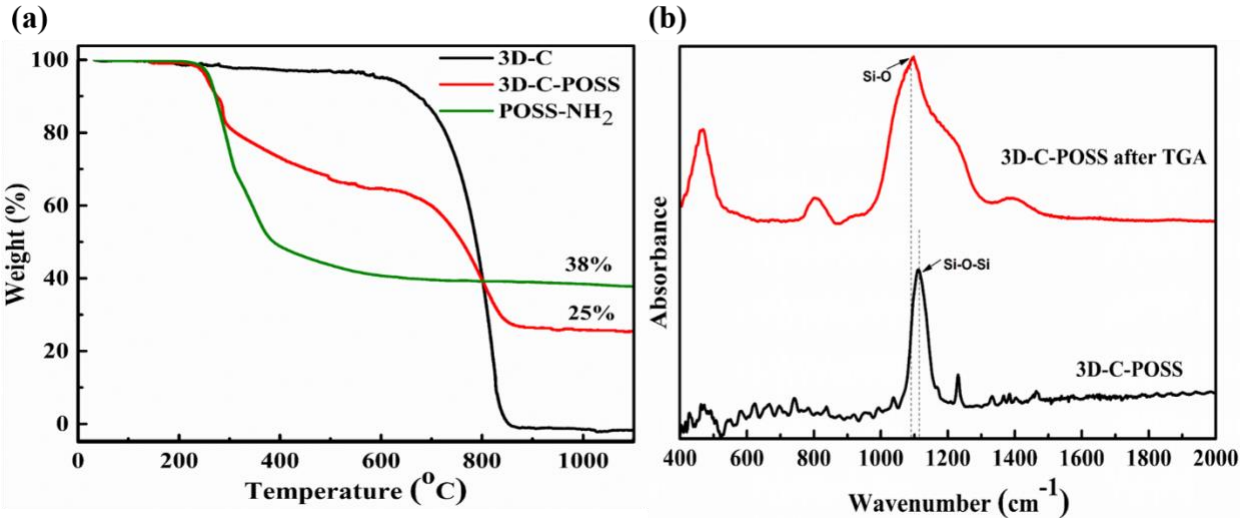

Figure 4. a) TGA curves of 3D-C (black), 3D-C-POSS (red) and POSS-NH_2 (green) under dry air atmosphere, showing residual weight for both POSS-NH_2 and 3D-C-POSS due to highly

dense Si-O structure of POSS formed by partial crosslinking; b) FTIR spectra of 3D-C-POSS after TGA (red) treatment showing a broad band from Si-O stretching. The centre of the absorption band shifted to lower wavenumbers (1090 cm^{-1}) compared to FTIR absorbance peak of 3D-C-POSS before TGA (black) (1110 cm^{-1}) conforming the formation of Si-O structure during thermal degradation [67].

XPS measurements were performed to further validate the incorporation of POSS onto 3D-C. The elements and functional groups on the foam surface were examined. **Figure 5a** shows the XPS survey spectrum for the samples. 3D-C shows only C 1s (284 eV) peak along with very small trace of oxygen (O 1s peak). As expected, XP spectrum of POSS-NH_2 shows C 1s (284. 7 eV), O 1s (532 eV), N 1s (358.9 eV), Si 2p (101 eV) and Si 2s (151.7 eV) peaks. The appearance of Si 2p, Si 2s, and N 1s peaks along with increased O 1s peak in 3D-C-POSS with respect to 3D-C indicates that the POSS molecules are successfully incorporated on the 3D-C surface. The surface composition for 3D-C and 3D-C-POSS are summarized in **Table 1**. 3D-C foam is mainly composed of carbon with trace amounts of oxygen. After incorporation of POSS the carbon content decreased from 98.2 to 66.3% and elements such as nitrogen and silicon were seen accounting to 1.6% and 12.4%, respectively. The oxygen content also increased considerably from 1.8 to 19.7%. This increase in oxygen content is due to the Si-O-Si structure in the POSS cages. This is also reflected in the surface atomic ratio of O/C indicative of successful incorporation of POSS. **Figure 5b** and **5c** shows the high-resolution C 1s spectra for 3D-C-POSS and 3D-C, respectively. The C-C content of 3D-C was 87.22%, which decreased to 78.98% after adding POSS coating on its surface. Similarly, the C-O % in the 3D-C and 3D-C-POSS is 8.46 and 16.25, respectively. Thus, it is evident that the C-C content of the 3D-C foam decreased, and the C-O content increased considerably after adding POSS-NH_2.

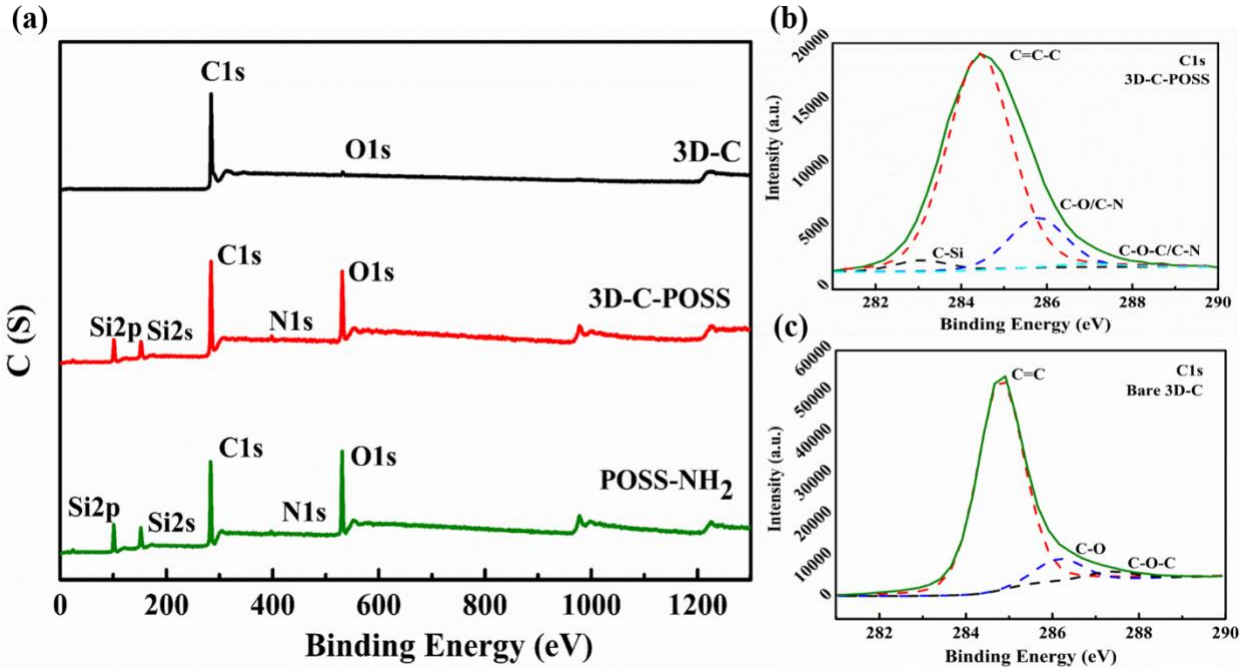

Figure 5. a) XPS survey spectra of the 3D-C, 3D-C-POSS, and POSS-NH_2 showing only C1s peak for pure 3D-C whereas the peaks of N1s (398.98 eV), Si 2p (101 eV), and Si 2s (152 eV) can be seen in both POSS and 3D-C-POSS indicating the successful incorporation of POSS onto 3D-C; b-c) High resolution C 1s spectra for 3D-C-POSS and 3D-C with their respective bonding modes obtained via deconvolution of the main signal.

Table 1. Surface element analysis of 3D-C and 3D-C-POSS foams

	Element Content (%)				
	C	O	N	Si	O/C
3D-C	98.2	1.8	---	---	0.018
3D-C-POSS	66.3	19.7	1.6	12.4	0.297

3.2. AO Durability

The composite films were exposed to AO, the dominant species in LEO altitudes. The films were subjected to AO fluences of $7.18 \times 10_{19}$ and $2.72 \times 10_{20}$ O-atoms/cm_2. AO fluence of $2.72 \times 10_{20}$ O-atoms/cm_2 is equivalent to about 5 months at an altitude of 500 Km [70]. **Figure 6a-c** shows the surface of the composite films before AO exposure. Good infusion of the PI in 3D-C can be seen for all the samples. Exposing 3D-C/PI and 3D-C-POSS/PI samples to $7.18 \times 10_{19}$ O

atoms/cm^2 resulted in erosion of the top PI matrix leaving the 3D-C network exposed, as seen in **Figure 6d** and **6e**. Before exposure only the top layer of 3D-C structure can be seen and after exposure the PI is etched away revealing several layers of 3D-C branches. This shows the lower AO erosion yield of 3D-C compared to that of PI as a result of strong carbon atoms bonding present in 3D-C. Similar results of relatively low erosion yield were previously reported for carbon structures, such as amorphous carbon or highly oriented pyrolytic graphite (HOPG) [5, 35, 71, 72]. Under the same AO fluence it can be seen that the PI layer of 3D-C-POSS/PI has been etched away creating small holes and increasing the roughness, whereas for 3D-C-POSS/PI-POSS and 3D-C/PI-POSS the PI top layer remained largely intact, as seen in **Figure 6f**. The samples exposed to a higher fluence of 2.72×10^{20} O-atoms/cm^2 showed a similar trend as visible in **Figure 6g-i**, where both sample containing POSS in the PI matrix experience the least damage to the PI phase compared to the samples with no POSS content in the PI. **Figure 6j** shows the damaged surface of the 3D-C/PI sample after the AO exposure at a higher magnification. The typical morphology of a PI surface damaged by hyperthermal AO is clearly seen [30]. While most of the damaged surface of the 3D-C-POSS/PI sample is similar to that of the 3D-C/PI surface, the extensive PI etching exposed the POSS covered 3D-C branches, as seen in **Figure 6k**. This POSS cover layer on the 3D-C prevents its surface from being completely exposed to AO. Unlike samples with no POSS content in the PI, both the 3D-C-POSS/PI-POSS and 3D-C/PI-POSS samples show relatively uniformly spread micron sized particles on the damaged PI surface, as seen in **Figure 6l**. These particles are most likely silica (SiO_2) produced from the oxidation process of the POSS. This has been verified previously for the same TSP-POSS/PI film exposed to AO fluence of 2.6×10^{20} O-atoms/cm^2 [73]. XPS survey spectra was obtained before and after the AO exposure. It was found that the carbon content decreased significantly, and the oxygen content increased, indicating the formation of SiO_2. Furthermore, high-resolution spectra of Si 2p peak indicated the oxidation of the POSS silicon oxide (Si/O=1/1.5) and the formation of SiO_2 (Si/O=1/2) passivation layer. Thus, under further exposure of 3D-C/PI-POSS and 3D-C-POSS/PI-POSS to higher AO fluences, the SiO_2 particles will eventually form a protective passivation layer on the PI preventing further etching from taking place.

The composite films with POSS in the PI matrix have enhanced resistance to AO as the silsesquioxane moiety ($RSiO_{1.5}$) reacts with the oxygen and forms a SiO_2 protective layer. The silicon in the PI surface gets oxidized to SiO_2, after exposure to O-atoms. Hence with increasing AO fluence, the organic content of the PI-POSS surface gets eroded and replaced by silica. The surface of the composite film becomes almost entirely SiO_2. This SiO_2 passivation layer ultimately limits the AO erosion rate [41].

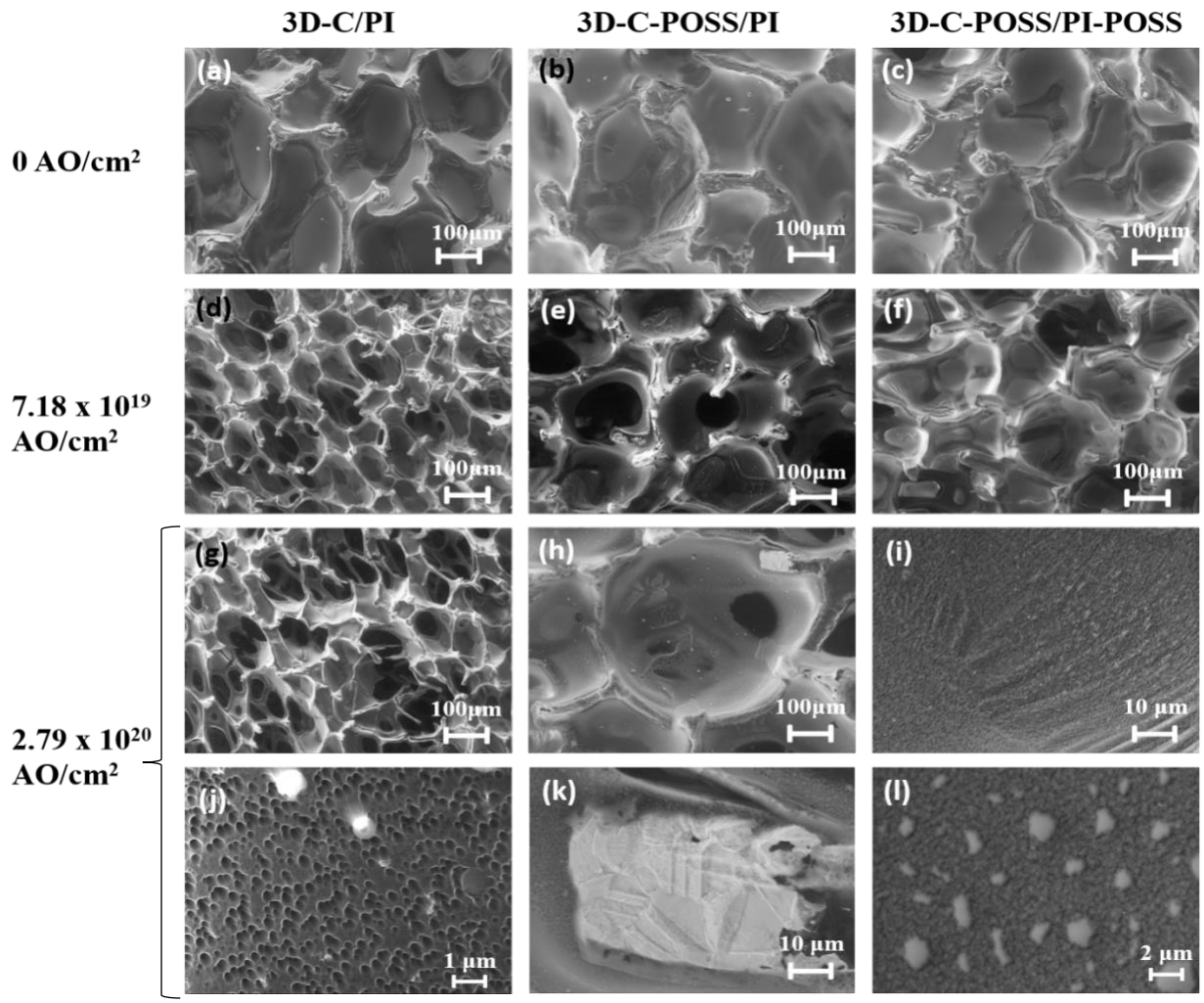

Figure 6 a-l. HRSEM images of three composite films (3D-D/PI, 3D-C-POSS/PI, 3D-C-POSS/PI-POSS) exposed to different AO fluences (0, $7.18 \times 10_{19}$, and $2.79 \times 10_{20}$ O atoms cm^{-2}) showing the effect of AO exposure in each composite films. SEM images of the 3D-C/PI-POSS before and after AO exposures show similar surface morphology to that of the 3D-C POSS/PI-POSS sample (not shown).

Mass loss of the composite films were measured after they were exposed to the AO fluence. **Figure 7a** shows the normalized mass loss measurements vs AO fluences and their linear fit. The erosion yield of the samples were obtained from the slope of the mass loss curves shown in **Figure 7a**, using equation (1). The results (**Figure 7b**) were compared to the accepted erosion yield of Kapton H which is 3.0×10^{-24} cm^3/O-atom [61]. It can be seen that the erosion yields of the two samples with no POSS content in the PI are similar, and their measured values are close to that measured for Kapton H. In contrast, the measured erosion yield of two samples with POSS content in the PI (15 wt%) are about 70%-80% lower than that of Kapton H.

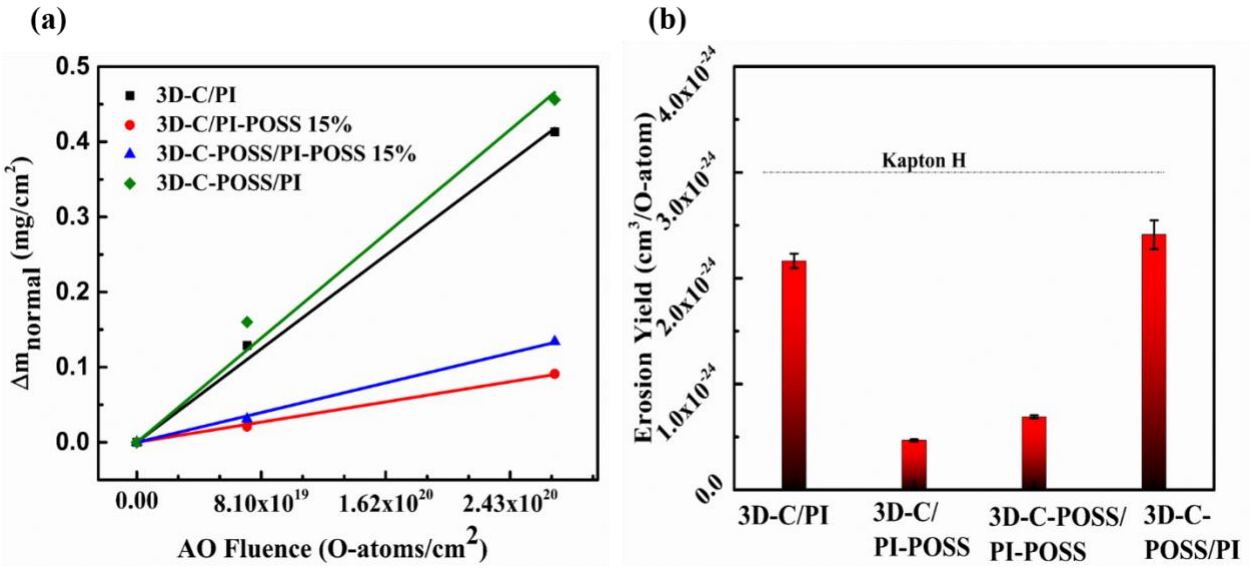

Figure 7. AO exposure test. a) Mass loss vs AO fluences for 3D-C/PI, 3D-C/PI-POSS, 3D-C-POSS/PI, and 3D-C-POSS/PI-POSS at three fluences (0, 7.18 × 10_{19}, and 2.72 × 10_{20} O-atoms/cm_2); b) Erosion yield of the samples obtained from mass loss and corresponding AO fluence.

The erosion yield of 3D-C/PI and 3D-C-POSS/PI were found to be 2.16 × 10_{-24} cm_3/O-atom and 2.4 × 10_{-24} cm_3/O-atom, respectively. Thus adding 3D-C to PI reduced the erosion yield (about 23% lower than Kapton H), mainly due to the lower erosion yield of the 3D-C compared to PI [27]. This is attributed to the strong bonding of carbon atoms in the foam compared to that of pure PI. Majority of mass loss in the composite samples are that of the PI which has an AO erosion yield about one order of magnitude higher than that of sp_2 carbon materials [5, 35, 71, 72]. Moreover, the measured erosion yield of 3D-C/PI-POSS and 3D-C-POSS/PI-POSS were found to be 4.67 × 10_{-25} cm_3/O-atom and 6.88 × 10_{-25} cm_3/O-atom, respectively. These values are about 60-70% lower than that measured for the 3D-C/PI and 3D-C samples that do not contain POSS in the PI. In addition, these values are 85 and 77% lower than the erosion yield of Kapton H, respectively.

LEO erosion time can be estimated assuming a layer thickness of 51 μm, equivalent to that of the outer layer of MLI blankets [6], and an AO flux of 2 × 10_{13} O-atoms/sec × cm_2 (AO flux at 500 km altitude) [70]. Hence based on the erosion yield measured, the film is estimated to be functional for about 15 years. The results show that protecting the PI by adding POSS reduces the composite film AO erosion yield. This is due to the fact that majority of the composite film mass is POSS-PI with reduced erosion yield compared to pristine PI. In addition, it is understood that adding POSS only as a coating on the 3D-C does not effectively protect the composite film, as it protects only the foam and does not prevent the PI from etching away.

3.3. Electrical Conductivity

Temperature dependent resistivity measurements were performed in order to investigate the effects of the addition of POSS to the composite films and the exposure to AO have on the embedded 3D-C conductivity, The measurements were made using the four-point van der Pauw method at temperatures ranging from -100 °C to 200 °C. Measurements were made before and after AO exposure and the sheet resistance plotted against temperature is shown in **Figure 8a-b**. $\ln(R_s T^{-1/2})$ is plotted against $T^{-1/4}$ as Arrhenius curves in the insert and fit with linear trend lines. The conduction behaviour of all the samples follow three-dimensional variable range hopping (VRH) behaviour. This behaviour was predicted by Godet [74] as due to the carriers hopping between energy levels within band-tails. The linear fitting lines of the VHR model by Godet [75] is shown in **Figure 8 c-d**. This conduction mechanism is described by the equation,

(3)
$$R_s(T) = R_{00} T^{\frac{1}{2}} exp\left(\left(\frac{T_0}{T}\right)^{\frac{1}{1+d}}\right)$$

Where, R_{00} - band tail's resistivity pre-factor
T_0 - Temperature coefficient containing the hopping parameters
d - Dimensionality of the hopping space

The hopping parameters are the density of the states and the localization length of the wave function. Here, it is seen that the results fit the VRH model with a temperature dependence of $T^{-1/4}$. The VRH model shows a temperature dependence of $\exp((T_0/T)^{1/(1+d)})$ and the data fits the expression $\exp((T_0/T)^{1/4})$ indicating that d = 3 and hence three dimensional electrical conduction in 3D-C based composites [76]. Similar electrical conductivity behaviour was reported earlier for both 3D-C and other carbon based materials [27, 35]. The temperature-dependent resistivity of all the samples (3D-C/PI, 3D-C-POSS/PI, 3D-C/PI-POSS and 3D-C-POSS/PI-POSS) follow the same trend with similar slopes signifying identical electrical conductivity properties. This is due to the fact that the electrical conductivity behaviour is mainly dependent on the intrinsic characteristic of the 3D-C foams. As seen in **Figure 8 a-b,** the resistivity curves for all the reference samples (red markings) are showing the same behaviour indicating that the addition of POSS to 3D-C and/or PI did not change or affect the electrical conductivity behaviour of the composite. In addition, the VRH conductivity mechanism is well preserved even after PI infiltration as well as adding POSS to the foam or PI.

The sheet resistance of the composite films exposed to a LEO equivalent AO fluences of $7.2 \times l0^{19}$ O-atoms/cm^2 (Figure 8a) and 2.7×10^{20} O-atoms/cm^2 (Figure 8b) were compared to the reference sample (before exposure) in order to examine their durability to AO fluences comparable to typical LEO spacecraft mission time. It can be seen that the sheet resistance of 3D-C/PI and 3D-C-POSS/PI have increased after each exposure while there is only a negligible change in the case of 3D-C/PI-POSS and 3D-C-POSS/PI-POSS. Moreover, it can be seen that the increase in sheet resistance measured for the 3D-C POSS/PI sample after exposure is lower than that measured for the 3D-C/PI sample. This is due to the added protection of the POSS covering the 3D-C and reducing the AO erosion.

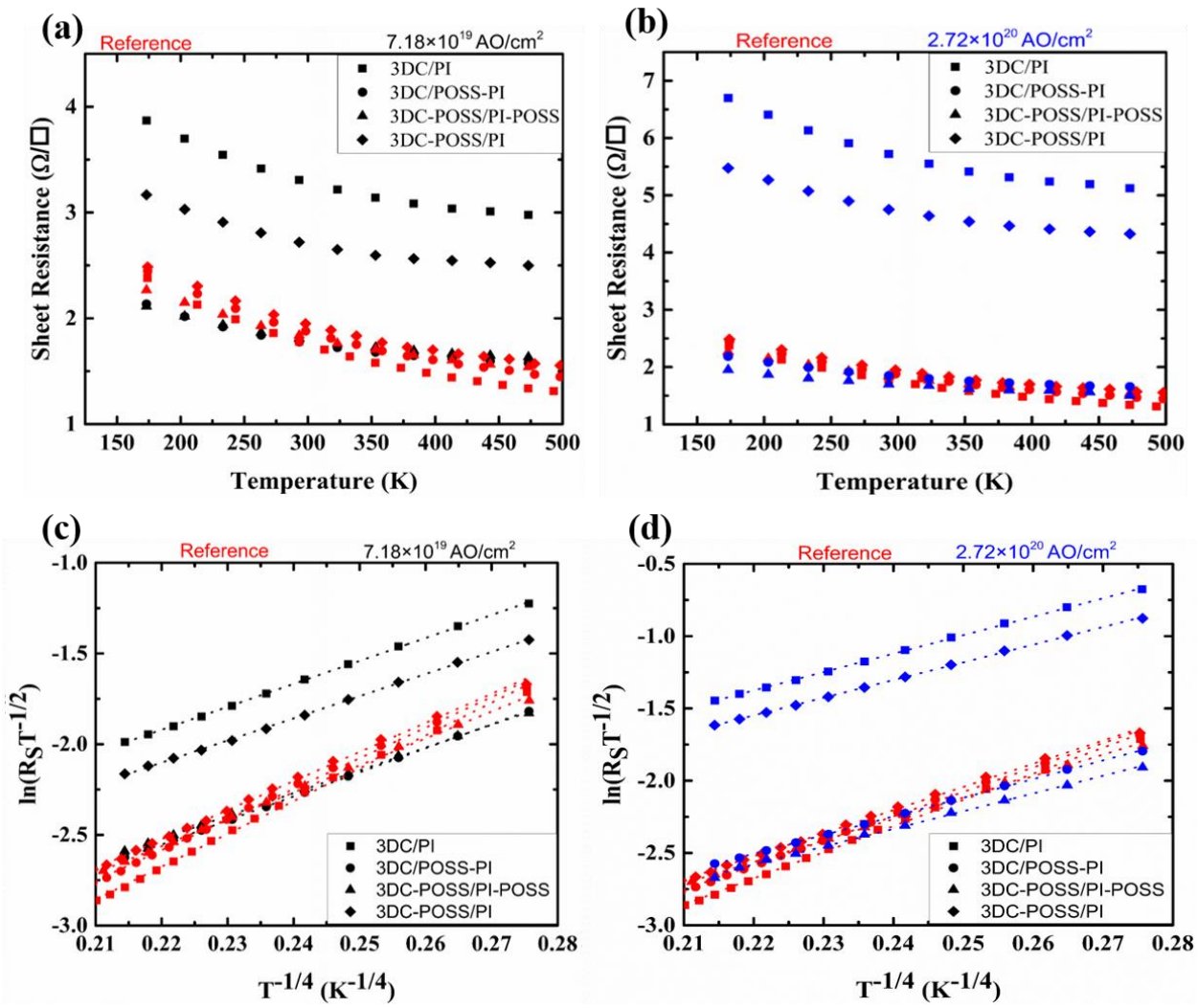

Figure 8. Electrical conductivity characterization before and after AO exposure. The sheet resistance as a function of temperature of the various samples after exposure, a) to a fluence of 7.18 × l0$_{19}$ O-atoms/cm$_2$ (black); b) a fluence of 2.72 × 10$_{20}$ O-atoms/cm$_2$ (blue) compared to the reference measurements performed on the samples before the exposure (red); c-d) Fitting of the sheet resistance measurements to the VRH conductivity model. Results are shown according to the VRH model: ln(R$_S$T$^{-1/2}$) as a function of T$^{-1/4}$ and compared to the model (dashed lines).

The VRH model was examined to gain further insight on the damage caused by AO to the 3D-C foams embedded in the PI. The conductivity by the VRH model according to Godet is given by equation [77].

(4)
$$\sigma(T) = \sigma_{00} T^{-\frac{1}{2}} exp\left(-\left(\frac{T_0}{T}\right)^{\frac{1}{1+d}}\right)$$

By transferring to resistivity (1/σ)= ρ, we get

(5) $$\rho(T) = \rho_{00} T^{\frac{1}{2}} exp\left(\left(\frac{T}{T_0}\right)^{-\frac{1}{1+d}}\right)$$

In the linear representation:

(6) $$ln\left(\rho T^{-\frac{1}{2}}\right) = ln(\rho_{00}) + \left(\frac{1}{T_0}\right)^{-\frac{1}{1+d}} T^{-\frac{1}{1+d}}$$

where ρ is the resistivity, T is the temperature, d is the dimensionality of the conductivity, T_o is a factor related to localization parameter, and ρ_{oo} is the exponential prefactor. ρ_{oo} is dependent on both lattice disorder and localization parameter. The correlation between localization parameter ($N(E_F)\ \gamma^{-3}$) and the T_o factor according to Goddet's VRH model is:

(7) $$310 = T_0 N(E_F) \gamma^{-3}$$

where $N(E_F)$ is the density of states in the Fermi level and γ^{-1} is the localization radius which equals the decay length of the electron wave function. Linear fitting was used to extract various parameters for each sample and each exposure. As reported earlier, the dimensionality *d* was found to be 3, indicating the multilayered structure of the 3D-C. Both the localization parameter and σ_{oo} of the different samples for AO exposures were extracted and compared, as seen in **Figure S3 and S4.**

It can be seen from **Figure S3,** that all localization parameters fall within the weak localization range, $l \times l0^{-5} \ll N(E_F)\gamma^{-3} \ll 1$. The extracted localization parameters are unaffected by the AO exposure. The localization parameter is proportional to the density of states in the graphene grain boundaries, where the hopping conductivity process takes place. This is attributed to the fact that majority of the AO induced defects are not located at the grain boundaries but on the surface of the top layer 3D-C grains themselves. Thus, no change in the hopping density of states and therefore the localization parameter is expected. Indeed, the results depicted in Figure S3, shows that all the samples retain roughly the same localization parameter value, regardless of POSS content or AO exposure fluence. However, the conductivity of the samples with no POSS content in PI were affected, most notably due to mobile charge scattering on the increased number of defects in the 3D-C grains. This is evident in the decrease in the σ_{oo} parameter which is dependent on the lattice disorder. As seen in **Figure S4**, the samples that did not contain any POSS in the PI matrix have a reduction in their σ_{oo} values indicating an increase in the 3D-C grains lattice disorder due to the AO damage. In summary, the composite samples without POSS in the PI shows an increase in the sheet resistance as a result of AO induced defects. These defects cause reduction in the conductivity and are probably limited to the outer layers of the multilayered 3D-C foam. The sheet resistance after exposure to 2.72×10^{20} O-atoms/cm^2 has increased by 200% to a value of 6 Ω/□. However, the location and density of the AO induced defects is still not enough to drastically change the conductivity mechanism. The samples with the POSS containing PI show no change in the measured sheet resistance, indicating that no AO penetrated the POSS protected PI. These results show that PI with POSS content (15 wt%) serves as an effective protection layer to the 3D-C embedded in the composite, preventing AO damage.

3.4. Mechanical Measurements

The stress strain curves obtained from the tension test is shown in **Figure 9a** and the results are summarized in **Table S1**. The results show that the adding of POSS to the PI matrix increases the Young's modulus of the composite by a measurable amount, as seen in **Table S1** and **Figure 9b**. The small size of POSS nano-cages, which restricts the mobility of polymer chains under loading, is predicted to improve the modulus and possibly the yield strength of PI-POSS compared to that of pure PI. This effect was documented in previous work conducted on PI and various POSS types, showing that an increase of POSS concentration would lead to an increase in the rigidity of the composite system [78]. In addition, previous work indicate that a POSS loading of 15 wt.% will lead to a reduction in the PI mechanical properties compared to that of PI with a POSS loading of 5 wt.% [60]. This trend is visible in the decreased Modulus values measured for the 15 wt.% POSS loaded PI films as compared to the 5 wt.% POSS loaded films. This is due to the formation of POSS aggregates at the 15 wt.% loading. These aggregates size and density affect the nanocomposite film mechanical properties [79].

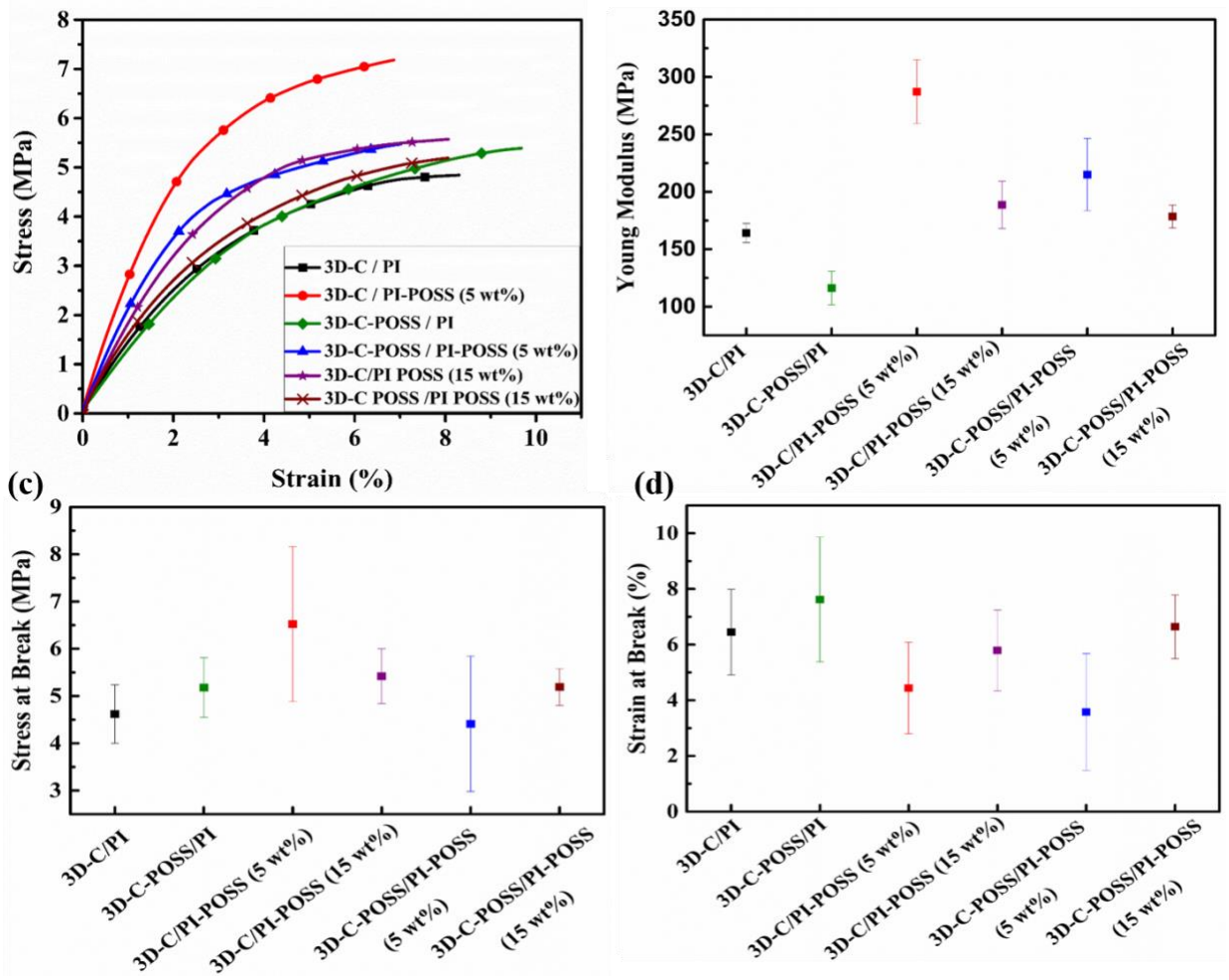

Figure 9. a) Stress – strain curves obtained from tension measurements on 4 types of samples. 3D-C/PI, 3D-C/PI-POSS (5 and 15 wt.%), 3D-C-POSS/PI, and 3D-C-POSS/PI-POSS (5 and 15

wt.%), b) The measured Young's modulus, (c) tensile strength, and (d) strain at break of the 6 sample types. Each result is an average of the at least five measured samples.

In contrast, adding POSS as a coating to the 3D-C structure has the opposite effect, reducing the Young's modulus slightly compared to that of the untreated composite material. This result is expected as the POSS coating was found to have no chemical bonding to the 3D-C structure and therefore decreases the adhesion of the PI to the 3D-C surface reducing the stiffness of the composite. The measured tensile strength and strain at break was found to be similar in all the sample types without correlation to the POSS content, as seen in **Table S1** and **Figure 9.** This is contrary to previous works that show an increase in the tensile strength of PI with a POSS content of 5 %wt. compared to bare PI [60, 78]. This may be due a lower than expected PI volume filling in the composite films.

The measured proprieties for the 3D-C/PI composite films are considerably lower than those of a pure PI film. The Young's modulus of pure PI films prepared in the same way as the PI infused into the 3D-C was measured and found to be roughly 2 GPa, one order of magnitude higher than that of the various 3D-C/PI films. This large variation in mechanical properties between the composite films and their equivalent PI films indicates the existence of voids in the composite film structure (regardless of the POSS content in the material used). This non-uniformity in PI infiltration into the 3D-C scaffolding can clearly be seen in SEM images of the 3D-C PI films cross section. Typical SEM images, such as the one depicted in **Figure 10a,** clearly show the lack of PI matrix material in the middle of the film. In addition, the images clearly show that the PI did not infiltrate inside the hollow 3D-C structure (**Figure 10b**). Furthermore, delamination between the 3D-C structure and the PI matrix can be seen in the interface area between the two materials. Thus, indicating the lack of proper adhesion which is the result of the weak physicals bonds and the lack of any chemical bonding between the 3D-C and PI matrix.

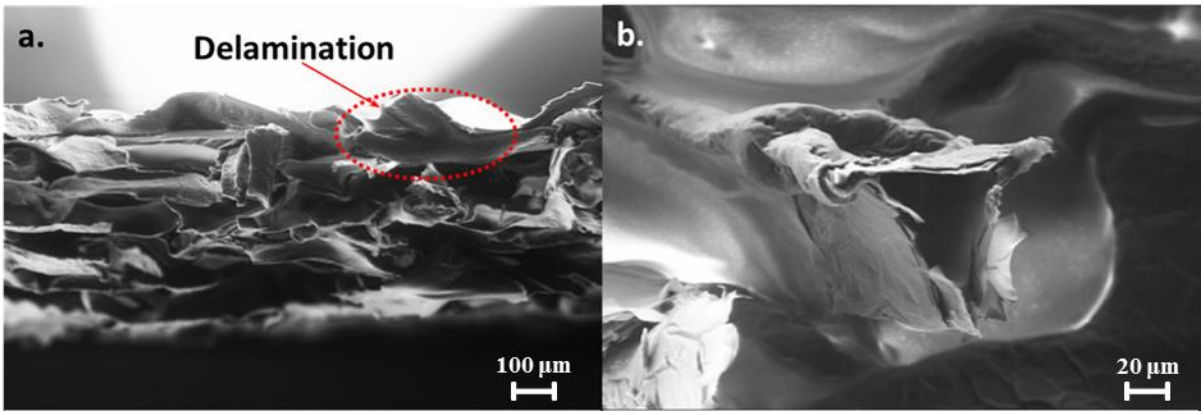

Figure 10. SEM images of a cleaved 3D-C/PI composite film. a) A delamination between the 3D-C scaffolding and the PI matrix is clearly visible in the area marked by a dotted red line; b) Cross section of the 3D-C scaffolding structure. While a PI cover is seen on the outer surface of the 3D-C structure, the inside remained hollow. This indicates that the PI failed to infiltrate inside the hollow 3D-C structure.

These results show that these composite samples are still suited for use as the outer layer in thermal blankets in satellites as they undergo mostly bending and are supported by the multi-layered structure of the blanket. For other applications further optimization of the PI matrix should be explored, alternative PI based matrix materials should be considered in order to further increase the adhesion of the 3D-C scaffolding to the PI matrix, thereby improving the composite film mechanical properties. Several alternative polymer matrix materials have been considered and preliminary results are promising.

4. Summary and Conclusion

The current study reports the synthesis of different 3D-C/PI based composite films by adding POSS to 3D-C and/or PI and a comparison of the impact of POSS on the electrical and mechanical properties along with their AO durability for LEO applications. The electrical conductivity behaviour of all the composite films is mainly dependent on the intrinsic characteristic of the 3D-foams and it is well preserved even after PI infiltration as well as adding POSS to the foam or PI. This is evident from the similar slopes followed by temperature-dependent resistivity of all the samples. The composite films demonstrated sheet resistivity as low as 1.8 Ω/□ at room temperature. The samples were also subjected to the LEO equivalent hyperthermal (5 eV) AO fluences of $7.18 \times l0_{19}$ O-atoms/cm$_2$ and $2.72 \times 10_{20}$ O-atoms/cm$_2$. The 3D-C/PI composite samples without POSS content in the PI matrix exhibited an erosion yield close to that of Kapton H (23% lower). On the other hand, the erosion yield values of the samples with POSS content (15 wt%) in the PI matrix were measured to be 77 to 85% lower than that of pure PI Kapton H. The electrical conductivity of the films with POSS in PI was found to be well-maintained even after AO exposure. For 3D-C/PI and 3D-C-POSS/PI an increase in the sheet resistance was measured as a result of AO exposure. However, the total conductivity is still very high indicating that the defect induced conductivity reduction is limited to the outer layers of the multilayer 3D-C foam. Adding POSS to the 3D-C foam reduced the Young's modulus of the material, while adding 5 wt% POSS to the PI increases it. However, adding 15 wt% to the PI increases the AO protection but have reduced benefit to mechanical properties compared to 5 wt% loading.

In conclusion, adding POSS as a coating to 3D-C alone does not seem to have any significant effect on the composite erosion yield. This is expected since the majority of the film mass is PI and so films with unprotected PI will show an erosion yield similar to pure PI films. In terms of stiffness, 3D-C/PI-POSS has the highest Young's modulus followed by 3D-C-POSS/PI-POSS, 3D-C/PI and 3D-C-POSS/PI. The results indicate that POSS in PI prevents AO erosion in the films with no detrimental effect on the electrical conductivity characteristics of the 3D-C material. The study shows that, adding 15 wt% POSS content to the PI matrix drastically improves the durability of the 3D-C/PI composite to AO. Thus, making 3D-C/PI-POSS composite films with a POSS content of 15 wt% in the polymer matrix a promising material for LEO space applications.

Acknowledgements

The authors would like to thank Prof. Rafi Kalish and Dr. Moshe Tordjman (Solid State Institute, Technion, Israel) for the use of VDP Hall/sheet resistance measurement system.

References

[1] J. Chen, N. Ding, Z. Li, W. Wang, Organic polymer materials in the space environment, Prog. Aerosp. Sci., 83 (2016), 37-56. https://doi.org/10.1016/j.paerosci.2016.02.002.

[2] L.W. Townsend, R.J.M Fry, Radiation protection guidance for activities in low-Earth orbit, Adv. Space Res., 30 (4) (2002), 957-963. https://doi.org/10.1016/S0273-1177(02)00160-6.

[3] R.K. Tripathi, J.W. Wilson, R.C. Youngquist, Electrostatic space radiation shielding, Adv. Space Res., 42(6) (2008), 1043-1049. https://doi.org/10.1016/j.asr.2007.09.015.

[4] P. Spillantini, Active shielding for long duration interplanetary manned missions, Adv. Space Res., 45(7) (2010), 900-916. https://doi.org/10.1016/j.asr.2010.01.025.

[5] A.C. Tribble, The space environment : implications for spacecraft design, Princeton, N.J. ; Woodstock : Princeton University Press, 2003. Rev. and expanded ed.2003.

[6] M.D. Finckenor, D. Dooling, Multilayer Insulation Material Guidelines, NASA/TP-1999-209263, National Aeronautics and Spcae Administration, Washington, D.C., 1999.

[7] M.K. Ghosh, K.L. Mittal, Polyimides : fundamentals and applications, New York : M. Dekker, 1996.

[8] M.R. Reddy, N. Srinivasamurthy, B.L. Agrawal, Atomic Oxygen Protective Coatings for Kapton Film - A Review, Surf. Coat. Tech., 58(1) (1993), 1-17. https://doi.org/10.1016/0257-8972(93)90169-O.

[9] B.A. Banks, A. Snyder, S.K. Miller, K.K. de Groh, R. Demko, Atomic-oxygen undercutting of protected polymers in low earth orbit, J. Spacecraft Rockets, 41(3) (2004), 335-339. https://doi.org/10.2514/1.10726.

[10] D. Angirasa, P.S. Ayyaswamy, Review of Evaluation Methodologies for Satellite Exterior Materials in Low Earth Orbit, J. Spacecraft Rockets, 51(3) (2014), 750-761. https://doi.org/10.2514/1.A32742.

[11] K. Gotlib-Vainstein, I. Gouzman, O. Girshevitz, A. Bolker, N. Atar, E. Grossman, C.N. Sukenik, Liquid Phase Deposition of a Space-Durable, Antistatic SnO2 Coating on Kapton, ACS Appl. Mater. Inter., 7(6) (2015), 3539-3546. https://doi.org/10.1021/am5072817.

[12] D.R. Cairns, R.P. Witte, D.K. Sparacin, S.M. Sachsman, D.C. Paine, G.P. Crawford, R.R. Newton, Strain-dependent electrical resistance of tin-doped indium oxide on polymer substrates, Appl. Phys. Lett., 76(11) (2000), 1425-1427. https://doi.org/10.1063/1.126052.

[13] P. George, Space Environmental Effects on LDEF Low Earth Orbit Exposed Graphite Reinforced Polymer Matrix Composites, NASA Conf. P., 3162 (1992) 543-570.

[14] H. Fong, R.A. Vaia, J.H. Sanders, D. Lincoln, A.J. Vreugdenhil, W. Liu, J. Bultman, C. Chen, Self-Passivation of Polymer-Layered Silicate Nanocomposites, Chem. Mater., 13(11) (2001), 4123-4129. https://doi.org/10.1021/cm010150o.

[15] S. Yagnamurthy, Q. Chen, C. Chen, I. Chasiotis, Erosion yield of epoxy–silica nanocomposites at the lower earth orbit environment of the International Space Station, J. Compos. Mater., 47(1) (2012), 107-117. https://doi.org/10.1177/0021998312442558.

[16] R.L. Kiefer, R.A. Orwoll, E.C. Aquino, A.C. Pierce, M.B. Glasgow, S.A. Thibeault, The effects of atomic oxygen on polymer films containing bis(triphenyltin) oxide, Polym. Degrad. Stabil., 57(2) (1997), 219-226. https://doi.org/10.1016/S0141-3910(97)00003-7.

[17] K.A. Watson, F.L. Palmieri, J.W. Connell, Space Environmentally Stable Polyimides and Copolyimides Derived from [2,4-Bis(3-aminophenoxy)phenyl]diphenylphosphine Oxide, Macromolecules, 35(13) (2002), 4968-4974. https://doi.org/10.1021/ma0201779.

[18] E. Miyazaki, M. Tagawa, K. Yokota, R. Yokota, Y. Kimoto, J. Ishizawa, Investigation into tolerance of polysiloxane-block-polyimide film against atomic oxygen, Acta Astronautica, 66 (5) (2010), 922-928. https://doi.org/10.1016/j.actaastro.2009.09.002.
[19] H.R. Fischer, K. Tempelaars, A. Kerpershoek, T. Dingemans, M. Iqbal, H. van Lonkhuyzen, B. Iwanowsky, C. Semprimoschnig, Development of Flexible LEO-Resistant PI Films for Space Applications Using a Self-Healing Mechanism by Surface-Directed Phase Separation of Block Copolymers, ACS Appl. Mater. Inter., 2(8) (2010), 2218-2225. https://doi.org/10.1021/am100223v.
[20] L.-C. Tang, Y.-J. Wan, D. Yan, Y.-B. Pei, L. Zhao, Y.-B. Li, L.-B. Wu, J.-X. Jiang, G.-Q. Lai, The effect of graphene dispersion on the mechanical properties of graphene/epoxy composites, Carbon, 60 (2013), 16-27. https://doi.org/10.1016/j.carbon.2013.03.050
[21] R. Prasher, Thermal interface materials: Historical perspective, status, and future directions, Proceedings of the IEEE, 94(8) (2006) 1571-1586. 10.1109/JPROC.2006.879796.
[22] M. Loeblein, R.Y. Tay, S.H. Tsang, W.B. Ng, E.H.T. Teo, Configurable Three-Dimensional Boron Nitride-Carbon Architecture and Its Tunable Electronic Behavior with Stable Thermal Performances, Small, 10(15) (2014), 2992-2999. https://doi.org/10.1002/smll.201400292.
[23] Z.P. Chen, W.C. Ren, L.B. Gao, B.L. Liu, S.F. Pei, H.M. Cheng, Three-dimensional flexible and conductive interconnected graphene networks grown by chemical vapour deposition, Nat. Mater., 10(6) (2011), 424-428. https://doi.org/10.1038/nmat3001.
[24] M.T. Pettes, H.X. Ji, R.S. Ruoff, L. Shi, Thermal Transport in Three-Dimensional Foam Architectures of Few-Layer Graphene and Ultrathin Graphite, Nano Lett., 12(6) (2012), 2959-2964. https://doi.org/10.1021/nl300662q.
[25] L. Zhang, M. Liu, S. Bi, L. Yang, S. Roy, X.-Z. Tang, C. Mu, X. Hu, Polydopamine decoration on 3D graphene foam and its electromagnetic interference shielding properties, J. Colloid. Interf. Sci., 493 (2017), 327-333. https://doi.org/10.1016/j.jcis.2017.01.046.
[26] Y. Wu, Z. Wang, X. Liu, X. Shen, Q. Zheng, Q. Xue, J.-K. Kim, Ultralight Graphene Foam/Conductive Polymer Composites for Exceptional Electromagnetic Interference Shielding, ACS Appl. Mater. Inter., 9(10) (2017) 9059-9069. https://doi.org/10.1021/acsami.7b01017.
[27] M. Loeblein, A. Bolker, S.H. Tsang, N. Atar, C. Uzan-Saguy, R. Verker, I. Gouzman, E. Grossman, E.H.T. Teo, 3D Graphene-Infused Polyimide with Enhanced Electrothermal Performance for Long-Term Flexible Space Applications, Small, 11(48) (2015), 6425-6434. https://doi.org/10.1002/smll.201502670.
[28] M.R. Reddy, Effect of Low-Earth-Orbit Atomic Oxygen on Spacecraft Materials, J. Mater. Sci., 30(2) (1995), 281-307. https://doi.org/10.1007/BF00354389.
[29] Z.A. Iskanderova, J.I. Kleiman, Y. Gudimenko, R.C. Tennyson, Generalization of the predictive model of erosion of carbon-based materials by atomic oxygen, Protection of Space Materials from the Space Environment, Space Technol. Proc., 4 (2001), 33-50. DOI: 10.1007/978-94-010-0714-6_3.
[30] E. Grossman, I. Gouzman, G. Lempert, Y. Noter, Y. Lifshitz, Assessment of Atomic-Oxygen Flux in Low-Earth-Orbit Ground Simulation Facilities, J. Spacecraft Rockets, 41(3) (2004), 356-359. https://doi.org/10.2514/1.10890.
[31] J.D. Froehlich, R. Young, T. Nakamura, Y. Ohmori, S. Li, A. Mochizuki, M. Lauters, G.E. Jabbour, Synthesis of multi-functional POSS emitters for OLED applications, Chem. Mater., 19(20) (2007), 4991-4997. https://doi.org/10.1021/cm070726v.

[32] Y.-L. Liu, M.-H. Fangchiang, Polyhedral oligomeric silsesquioxane nanocomposites exhibiting ultra-low dielectric constants through POSS orientation into lamellar structures, J. Mater. Chem., 19(22) (2009), 3643-3647. DOI: 10.1039/b900141g.
[33] R.Y. Kannan, H.J. Salacinski, J. De Groot, I. Clatworthy, L. Bozec, M. Horton, P.E. Butler, A.M. Seifalian, The antithrombogenic potential of a polyhedral oligomeric silsesquioxane (POSS) nanocomposite, Biomacromolecules, 7(1) (2006), 215-223. https://doi.org/10.1021/bm050590z.
[34] Y.L. Chu, C.C. Cheng, Y.P. Chen, Y.C. Yen, F.C. Chang, A new supramolecular POSS electroluminescent material, J. Mater. Chem., 22 (18) (2012), 9285-9292. DOI: 10.1039/C2JM00095D.
[35] N. Atar, E. Grossman, I. Gouzman, A. Bolker, V.J. Murray, B.C. Marshall, M. Qian, T.K. Minton, Y. Hanein, Atomic-Oxygen-Durable and Electrically-Conductive CNT-POSS-Polyimide Flexible Films for Space Applications, ACS Appl. Mater. Inter., 7(22) (2015), 12047-12056. https://doi.org/10.1021/acsami.5b02200.
[36] B. Viers, R.I. Gonzalez, S.H. Phillips, POSS Polymers for Space: Entrepreneurial Research, Air Force Research Lab Edwards AFB CA Propulsion Directorate, 2003.
[37] Y.Z. Liu, Y. Sun, F.L. Zeng, Q.H. Zhang, L. Geng, Characterization and analysis on atomic oxygen resistance of POSS/PVDF composites, Appl. Surf. Sci., 320 (2014), 908-913. https://doi.org/10.1016/j.apsusc.2014.09.121.
[38] T.K. Minton, M.E. Wright, S.J. Tomczak, S.A. Marquez, L.H. Shen, A.L. Brunsvold, R. Cooper, J.M. Zhang, V. Vij, A.J. Guenthner, B.J. Petteys, Atomic Oxygen Effects on POSS Polyimides in Low Earth Orbit, ACS Appl. Mater. Inter., 4(2) (2012), 492-502. https://doi.org/10.1021/am201509n.
[39] S.H. Phillips, T.S. Haddad, S.J. Tomczak, Developments in nanoscience: polyhedral silsesquioxane (POSS)-polymers oligomeric, Curr. Opin. Solid St. M., 8(1) (2004), 21-29. https://doi.org/10.1016/j.cossms.2004.03.002.
[40] M. Qian, V.J. Murray, W. Wei, B.C. Marshall, T.K. Minton, Resistance of POSS Polyimide Blends to Hyperthermal Atomic Oxygen Attack, ACS Appl. Mater. Inter., 8 (49) (2016), 33982-33992. https://doi.org/10.1021/acsami.6b10612.
[41] A.L. Brunsvold, T.K. Minton, I. Gouzman, E. Grossman, R. Gonzalez, An Investigation of the Resistance of Polyhedral Oligomeric Silsesquioxane Polyimide to Atomic-Oxygen Attack, High Perform. Polym., 16(2) (2004), 303-318. https://doi.org/10.1177/0954008304044121.
[42] Y.Q. Zhao, D.A. Schiraldi, Thermal and mechanical properties of polyhedral oligomeric silsesquioxane (POSS)/polycarbonate composites, Polymer, 46(25) (2005), 11640-11647. https://doi.org/10.1016/j.polymer.2005.09.070.
[43] G.Z. Li, L.C. Wang, H.L. Ni, C.U. Pittman, Polyhedral oligomeric silsesquioxane (POSS) polymers and copolymers: A review, J. Inorg. Organomet. P., 11(3) (2001) 123-154. https://doi.org/10.1023/A:1015287910502.
[44] B. Wu, Y. Zhang, D. Yang, Y. Yang, Q. Yu, L. Che, J. Liu, Self-Healing Anti-Atomic-Oxygen Phosphorus-Containing Polyimide Film via Molecular Level Incorporation of Nanocage Trisilanolphenyl POSS: Preparation and Characterization, Polymers, 11(6), (2019) 1013. DOI:10.3390/polym11061013.
[45] F. Zhao, Y.D. Huang, Preparation and properties of polyhedral oligomeric silsesquioxane and carbon nanotube grafted carbon fiber hierarchical reinforcing structure, J. Mater. Chem., 21(9) (2011), 2867-2870. https://doi.org/10.1039/C0JM03919E

[46] D. Wang, J. Liu, J.-F. Chen, L. Dai, Surface Functionalization of Carbon Dots with Polyhedral Oligomeric Silsesquioxane (POSS) for Multifunctional Applications, Adv. Mater. Interfaces, 3(1) (2016) 1500439. **https://doi.org/10.1002/admi.201500439**.
[47] L. Valentini, S.B. Bon, M. Cardinali, O. Monticelli, J.M. Kenny, POSS vapor grafting on graphene oxide film, Chem. Phys. Lett., 537 (2012), 84-87. https://doi.org/10.1016/j.cplett.2012.04.016.
[48] H. Mahfuz, F. Powell, R. Granata, M. Hosur, M. Khan, Coating of Carbon Fiber with Polyhedral Oligomeric Silsesquioxane (POSS) to Enhance Mechanical Properties and Durability of Carbon/Vinyl Ester Composites, Materials, 4(9) (2011), 1619-1631. https://doi.org/10.3390/ma4091619.
[49] A. Gomathi, K. Gopalakrishnan, C.N.R. Rao, Covalent functionalization of metal oxide and carbon nanostructures with polyoctasilsesquioxane (POSS) and their incorporation in polymer composites, Mater. Res. Bull., 45(12) (2010), 1894-1898. https://doi.org/10.1016/j.materresbull.2010.09.001.
[50] D.J. Clarke, J.G. Matisons, G.R. Simon, M. Samoc, A. Samoc, Polyhedral oligomeric silsesquioxane bound fulleropyrrolidines, Appl. Organomet. Chem., 22(8) (2008), 460-465. https://doi.org/10.1002/aoc.1425.
[51] A. Tan, S.Y. Madani, J. Rajadas, G. Pastorin, A.M. Seifalian, Synergistic photothermal ablative effects of functionalizing carbon nanotubes with a POSS-PCU nanocomposite polymer, J. Nanobiotechnol., 10, 34 (2012). https://doi.org/10.1186/1477-3155-10-34.
[52] G. Potsi, A. Rossos, A. Kouloumpis, M.K. Antoniou, K. Spyrou, M.A. Karakassides, D. Gournis, P. Rudolf, Carbon Nanostructures Containing Polyhedral Oligomeric Silsesquioxanes (POSS), Curr. Org. Chem., 20(6) (2016), 662-673. DOI: 10.2174/1385272819666151006010352.
[53] D. Gnanasekaran, K. Madhavan, B.S.R. Reddy, Developments of polyhedral oligomeric silsesquioxanes (POSS), POSS nanocomposites and their applications: A review, JSIR, 68(6) (2009), 437-464.
[54] F. An, C. Lu, Y. Li, J. Guo, X. Lu, H. Lu, S. He, Y. Yang, Preparation and characterization of carbon nanotube-hybridized carbon fiber to reinforce epoxy composite, Materials & Design, 33 (2012), 197-202. https://doi.org/10.1016/j.matdes.2011.07.027.
[55] S.J. See, S.H. Han, K.U. Jeong, I.J. Bae, I.P. Hong, S.K. Choi, S.S. Kim, Effect of crystal morphology transition of polypropylene on interfacial properties of carbon fiber-reinforced composites through AlOOH surface treatment, Compos. Part A-Appl S., 78 (2015), 362-370. https://doi.org/10.1016/j.compositesa.2015.08.036.
[56] N. Atar, E. Grossman, I. Gouzman, A. Bolker, Y. Hanein, Reinforced Carbon Nanotubes as Electrically Conducting and Flexible Films for Space Applications, ACS Appl. Mater. Inter., 6(22) (2014), 20400-20407. https://doi.org/10.1021/am505811g.
[57] Z. Jiang, H. Zhang, Z. Zhang, H. Murayama, K. Okamoto, Improved bonding between PAN-based carbon fibers and fullerene-modified epoxy matrix, Compos. Part A-Appl. S., 39(11) (2008), 1762-1767. https://doi.org/10.1016/j.compositesa.2008.08.005.
[58] W.-H. Liao, H.-W. Tien, S.-T. Hsiao, S.-M. Li, Y.-S. Wang, Y.-L. Huang, S.-Y. Yang, C.-C.M. Ma, Y.-F. Wut, Effects of Multiwalled Carbon Nanotubes Functionalization on the Morphology and Mechanical and Thermal Properties of Carbon Fiber/Vinyl Ester Composites, ACS Appl. Mater. Inter., 5(9) (2013), 3975-3982. https://doi.org/10.1021/am400811p.
[59] G.S. Wu, L.C. Ma, L. Liu, Y.W. Wang, F. Xie, Z.X. Zhong, M. Zhao, B. Jiang, Y.D. Huang, Interface enhancement of carbon fiber reinforced methylphenylsilicone resin composites

modified with silanized carbon nanotubes, Materials & Design, 89 (2016), 1343-1349. https://doi.org/10.1016/j.matdes.2015.10.016.
[60] R. Verker, E. Grossman, N. Eliaz, Erosion of POSS-polyimide films under hypervelocity impact and atomic oxygen: The role of mechanical properties at elevated temperatures, Acta Mater., 57(4) (2009), 1112-1119. https://doi.org/10.1016/j.actamat.2008.10.054.
[61] D.M. Buczala, A.L. Brunsvold, T.K. Minton, Erosion of Kapton® H by hyperthermal atomic oxygen, J. Spacecraft. Rockets, 43(2) (2006), 421-425. https://doi.org/10.2514/1.16402.
[62] ASTM E2089 - 15, Standard Practices for Ground Laboratory Atomic Oxygen Interaction Evaluation of Materials for Space Applications, ASTM International, West Conshohocken, PA, 2015. DOI: 10.1520/E2089-15.
[63] L.J. van der Pauw, A method of measuring specific resistivity and Hall effect of discs of arbitrary shape, Philips Res. Repts, 13(1) (1958), 1-9.
[64] Y.H. Xue, Y. Liu, F. Lu, J. Qu, H. Chen, L.M. Dai, Functionalization of Graphene Oxide with Polyhedral Oligomeric Silsesquioxane (POSS) for Multifunctional Applications, J. Phys. Chem. Lett., 3(12) (2012), 1607-1612. https://doi.org/10.1021/jz3005877.
[65] A.C. Ferrari, J.C. Meyer, V. Scardaci, C. Casiraghi, M. Lazzeri, F. Mauri, S. Piscanec, D. Jiang, K.S. Novoselov, S. Roth, A.K. Geim, Raman spectrum of graphene and graphene layers, Phys. Rev. Lett., 97(18) (2006), 187401. https://doi.org/10.1103/PhysRevLett.97.187401.
[66] D. Yoon, H. Moon, H. Cheong, J.S. Choi, J.A. Choi, B.H. Park, Variations in the Raman Spectrum as a Function of the Number of Graphene Layers, J Korean Phys. Soc., 55(3) (2009), 1299-1303. https://doi.org/10.3938/jkps.55.1299.
[67] A. Fina, D. Tabuani, F. Carniato, A. Frache, E. Boccaleri, G. Camino, Polyhedral oligomeric silsesquioxanes (POSS) thermal degradation, Thermochim. Acta, 440(1) (2006), 36-42. https://doi.org/10.1016/j.tca.2005.10.006.
[68] S. Chabi, Electrochemical study of 3D graphene composites and the creation of ultralight 3D SiC, (2015). http://hdl.handle.net/10871/18502.
[69] M. Le Bras, Fire retardancy of polymers: new applications of mineral fillers, Cambridge, UK : Royal Society of Chemistry, 2005.
[70] D.R. Peplinski, Arnold, G. S., Borson, E. N., Introduction to Simulation of Upper Atmosphere Oxygen Satellite Exposed to Atomic Oxygen in Low Earth Orbit, 13th Space Simulation Conference, 1984, 133-145.
[71] R.E. Camacho, A.R. Morgan, M.C. Flores, T.A. McLeod, V.S. Kumsomboone, B.J. Mordecai, R. Bhattacharjea, W. Tong, B.K. Wagner, J.D. Flicker, S.P. Turano, W.J. Ready, Carbon nanotube arrays for photovoltaic applications, JOM, 59(3) (2007), 39-42. https://doi.org/10.1007/s11837-007-0037-0.
[72] K.T. Nicholson, T.K. Minton, S.J. Sibener, Temperature-dependent morphological evolution of HOPG graphite upon exposure to hyperthermal O(3P) atoms, Prog. Org. Coat., 47(3-4) (2003), 443-447. https://doi.org/10.1016/S0300-9440(03)00134-6.
[73] R. Verker, E. Grossman, I. Gouzman, N. Eliaz, POSS-Polyimide Nanocomposite Films: Simulated Hypervelocity Space Debris and Atomic Oxygen Effects, High Perform. Polym., 20(4-5) (2008), 475-491. https://doi.org/10.1177/0954008308089710.
[74] C. Godet, Physics of bandtail hopping in disordered carbons, Diam. Relat. Mater., 12(2) (2003), 159-165. https://doi.org/10.1016/S0925-9635(03)00017-7.
[75] C. Godet, Hopping model for charge transport in amorphous carbon, Philos. Mag. B, 81(2) (2001), 205-222. https://doi.org/10.1080/13642810108216536.

[76] L. Gan, A. Bolker, C. Saguy, R. Kalish, D.L. Tan, B.K. Tay, D. Gruen, P. Bruno, The effect of grain boundaries and adsorbates on the electrical properties of hydrogenated ultra nano crystalline diamond, Diam. Relat. Mater., 18(9) (2009), 1118-1122. https://doi.org/10.1016/j.diamond.2009.02.023.
[77] C. Godet, Variable range hopping revisited: the case of an exponential distribution of localized states, J. Non-Cryst. Solids, 299-302(Part-1) (2002), 333-338. https://doi.org/10.1016/S0022-3093(01)01008-0.
[78] J.-c. Huang, C.-b. He, Y. Xiao, K.Y. Mya, J. Dai, Y.P. Siow, Polyimide/POSS nanocomposites: interfacial interaction, thermal properties and mechanical properties, Polymer, 44(16) (2003) ,4491-4499. https://doi.org/10.1016/S0032-3861(03)00434-8.
[79] R. Verker, E. Grossman, N. Eliaz, Effect of the POSS-Polyimide nanostructure on its mechanical and electrical properties, Compos. Sci. Technol., 72(12) (2012), 1408-1415. https://doi.org/10.1016/j.compscitech.2012.05.014.